A structural view of Pd model catalysts : high-pressure surface X-Ray diffraction

Rijn, R. van

Chapter 5

CO oxidation and reaction oscillations on Pd nanoparticles

In this chapter we describe the results of a structure and reactivity study of supported Pd nanoparticles under conditions relevant for CO oxidation. Observations of reaction oscillations on these Pd nanoparticles are extensively discussed. We show that the reaction rate oscillations on the nanoparticles follow a similar oxidation-reduction mechanism as those on the extended Pd(100) single-crystal surface. We also show that interface compounds between the particles and the substrates are present.

In preparation for publication: *Reaction Oscillations on Pd nanoparticles*,
R. van Rijn, O. Balmes, M. E. Cañas Ventura, M. E. Messing, A. Resta, D. Wermeille R. Westerström, K. Deppert, R. Felici, E. Lundgren, and J. W. M. Frenken.

5.1 Introduction

Reaction rate oscillations are known to occur in many different systems in homogeneous as well as heterogeneous reactions. The Belousov-Zhabotinsky reaction and the Briggs-Rauscher reaction are the most famous examples in the case of homogeneous reactions in a solution, due to the spectacular spontaneous colour changes of the solution [107, 108]. In the case of heterogeneous catalysis one can also find oscillating reactions, a famous example being the work by Ertl on the self-sustained oscillations in the CO oxidation rate on metal surfaces, at both low and high pressures [94]. Reaction oscillations are not restricted to single-crystal surfaces [72], but also occur on supported nanoparticle catalysts [109]. For the latter systems, oscillations have mainly been measured using gas analysis and spectroscopic techniques [110]. It was also shown that oscillations occur in a real car catalyst [111].

Supported nanoparticles make up a much more intricate system than single crystal model catalysts. Even on a single face of a single crystal, multiple oxides can exist, as shown in Chapter 3. A nanoparticle exposes multiple facets to the reactant gases, but also edges and corners. The relative densities of these different sites change with particle size. Furthermore, a nanoparticle can also have a significant interaction with the supporting material. All these extra ingredients can have an influence on the thermodynamics and kinetics of oxide formation.

Several detailed studies have been performed of the oxidation of epitaxially aligned Pd and Rh particles [25, 112]. Size-dependent oxidation of Pd supported on Fe_3O_4 has been studied using molecular beams and STM [113]. Oxidation of Al_2O_3 supported Pd nanoparticles has been studied using FTIR, XRD and DFT [114]. The role played by the different oxides in the activity of the particles towards CO oxidation remains a topic of discussion also for Pt and Pd particles [110, 114–118].

In this chapter we will analyse the shape and crystal structure of supported Pd nanoparticles in situ and during spontaneous reaction oscillations. We use XRD to determine whether (bulk) PdO is present under various P_{O_2}/P_{CO} ratios and at different temperatures relevant for CO oxidation. Simultaneously, we monitor the CO_2 production by mass spectrometry. Then, we study the particles while the CO_2 production shows spontaneous oscillations under constant temperatures and gas flow. We again use XRD to determine the presence of PdO during the oscillations. We use GISAXS as an additional tool to determine the average particle

dimensions during the oscillations [11].

5.2 Experimental methods

Pd nanoparticles with a radius of 15 nm were created using a spark discharge method followed by size selection and annealing [119]. Subsequently the particles were deposited on two different substrates, SiO_2 and α-Al_2O_3(0001). This sample preparation ensures a narrow size distribution of the particles with a relative standard deviation of $\frac{\sigma_R}{R} = 0.05$, allowing us to accurately determine the average particle size. The number density of the particles was approximately $7 \times 10^2\,\mu m^{-2}$. However the particles are deposited at random positions on the substrate and their crystal structure is not epitaxially aligned with the substrate crystal structure. This is different from the case of epitaxial Pd nanoparticles obtained by Pd deposition on MgO(100) [25, 120, 121].

The samples were used in the XRD and GISAXS experiment in the flow setup without further preparation steps. Samples were mounted on a tungsten plate supported on a bora-electric heater described in Chapter 2. A type-C thermocouple was pressed against the tungsten plate supporting the sample.

All experiments were performed at the ID03 beamline at the ESRF. We used a focused beam of 18 keV x-rays (5×10^{12} photons s^{-1}, 200 mA ring current). For the GISAXS experiments, 500 µm anti-scattering slits were placed just before the Be dome. Ideally one would use a beamstop between the sample and the Be exit windows to prevent scattering from the exit window. The small space between the Be dome and the sample forced us to perform the GISAXS experiments at a relatively high incidence angle of 0.7° instead. Note that by using this high incidence angle we effectively used the sample and supporting tungsten plate as a beamstop. The XRD experiments were performed at a 0.5° incidence angle. A maxipix 2D pixel detector was used to collect the diffracted x-rays [79–81].

5.3 Results and discussion

5.3.1 Reactivity and crystal structure

Figure 5.1 shows an Arrhenius plot of the reaction rate of the 15 nm Pd particles supported on SiO_2. For each P_{O_2}/P_{CO} ratio the reaction rate was measured

twice: once after pre-exposing the sample to pure oxygen for 45 s and once after pre-exposing the sample to pure CO 45 s. After the pre-exposure the sample was exposed to the desired P_{O_2}/P_{CO} for 250 s the gasflow through the reactor was stopped, turning the reactor into a batch reactor. Subsequently the reaction rate was determined from the initial slope of the mass 44 signal in the QMS. Since the difference between the pre-reduced and pre-oxidized datasets is small, we conclude that the pre-exposure has little influence on the active phase of the catalyst under the supplied reaction conditions. Note that for each reaction rate measurement at a specific temperature in Fig. 5.1 we pre-exposed the sample at that same specific temperature. Pre-exposing at a much higher temperature ($\geq$ 1073 K) might give very different results due to full oxidation of the particles [114]. For comparison with the data in Chapter 3 the turnover frequency (TOF) on the vertical axis of Fig. 5.1 is calculated by assuming that the sample has the same amount of reactive sites as a Pd(100) surface. The actual number of active sites on the particle sample can of course be very different. The apparent activation energy is changing over the low end of the measured temperature range in Fig. 5.1 from 0.71 eV at 650 K to 0.15 eV at 550 K for the pre-reduced dataset at $P_{O_2}/P_{CO} = 0.6$. This changing activation energy was reported in earlier studies [122, 123]. At high temperatures the TOF reaches a plateau at $\approx 200\,\text{molec site}^{-1}\,\text{s}^{-1}$. This value is precisely the same for the measurements on the Pd(100) crystal shown in Fig. 3.4 and corresponds to the mass transfer limit (MTL). We do observe however that the mass transfer limited reaction rate is reached for each P_{O_2}/P_{CO} ratio at a higher temperature for the particles than for the Pd(100) single-crystal surface. This can have two causes: firstly the real number of active sites on our NP sample is lower than on a single-crystal and secondly the temperature measurement might have a systematic error. This error in the temperature measurement is caused by the fact that the thermocouple actually measures the temperature of the plate supporting the sample. The sample temperature will thus be overestimated in case of a bad thermal contact between the plate and the sample.

Accompanying every data point in Fig. 5.1 we recorded the powder diffraction pattern from the particles. These patterns are shown in Fig. 5.2. The scans indicate that bulk PdO was only present at the highest temperatures at a P_{O_2}/P_{CO} of 2 and 10 and only if the sample was pre-oxidized. Based on our measurements on single-crystal Pd(100) in Chapter 3 we expect a surface oxide to be present on the particles in the other cases where the reactivity reaches the MTL. The detection

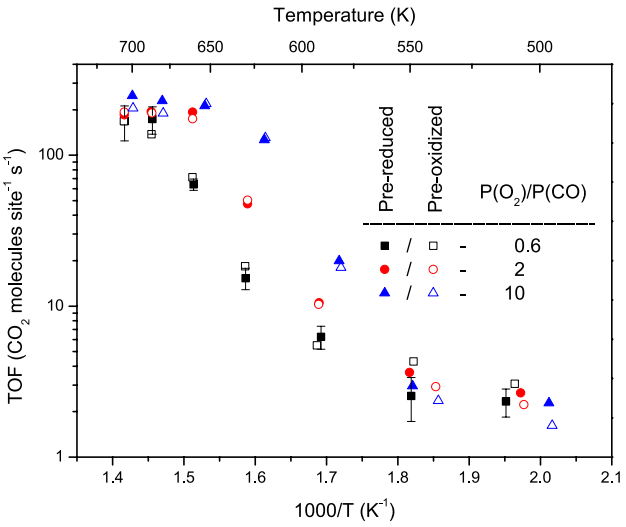

Figure 5.1: Arrhenius plot of the TOF for CO oxidation of the SiO_2-supported Pd nanoparticles of 15 nm diameter. For comparison with Fig. 3.4 the number of sites per unit of sample area is assumed to be equivalent to the number of sites on Pd(100). Data are shown for three different ratios between the partial pressure of O_2 and CO and for particles pre-exposed to either O_2 or CO prior to the TOF measurement. Representative error bars are shown for the pre-reduced dataset at $P_{O_2}/P_{CO} = 0.6$

of surface oxides remains challenging and this type of XRD scan is not sensitive to surface oxides. One could resort to epitaxially aligned nanoparticles for detection of surface oxides [112].However, in a first series of attempts with Pd particles on MgO(100) we have found that under catalytically relevant conditions the epitaxy of the particles was quickly lost.

Interestingly at lower temperatures ($< 550\,K$) we observe a decrease of the 2θ angle for the Pd(111) reflection if the nanoparticles are pre-reduced with CO. This points to a lattice expansion of the nanoparticles, likely caused by carbon dissolution [124–126].

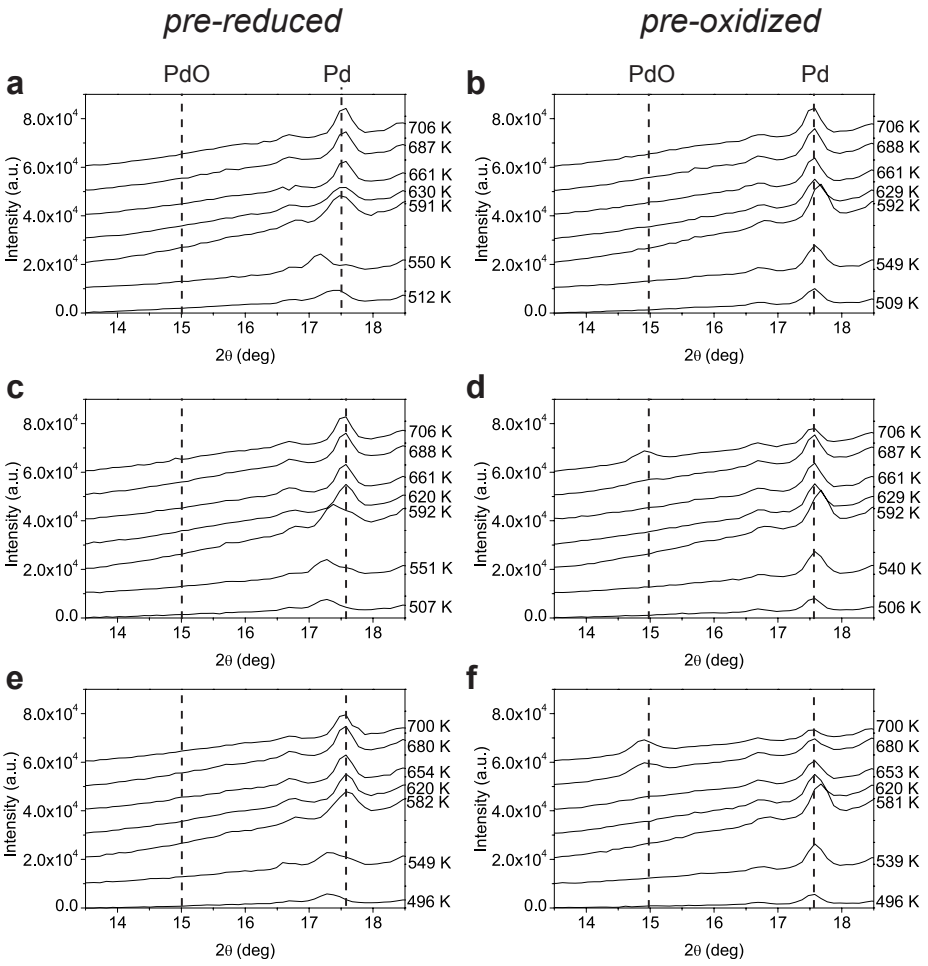

Figure 5.2: Powder diffraction patterns from the 15 nm Pd particles on SiO_2 for different temperatures at different gas conditions. **a),c)**, and **e)** show the results after the pre-reducing the particles with pure CO and then supplying $P_{O_2}/P_{CO} = 0.6$,2, and10 respectively. **b)**, **d)**, and **f)** show results after the pre-oxidizing the particles and then supplying at $P_{O_2}/P_{CO} = 0.6$, 2, and 10 respectively. Dotted lines indicate the theoretical position of the PdO(101) reflection at 15° and the Pd(111) reflection at 17.6°. We have not been able to identify the small peak at 16.7°, but it is likely coming from the substrate. Subsequent curves are offset by 10^4 a.u. for clarity.

5.3.2 Spontaneous reaction oscillations

SiO_2 support

Spontaneous oscillations of the reaction rate can be seen in Fig. 5.3. The diffracted intensity was measured at a 2θ angle of 17.6°. It shows that the amount of metallic Pd was oscillating with less metallic Pd present in the high CO_2 producing phase of the oscillations. Figure 5.4 shows the intensity of the PdO at a 2θ angle of 15° which is oscillating in antiphase with the Pd signal, confirming that a part of the Pd is converted to PdO. However during the oscillations on the particles the amount of PdO never reduces to zero during the low CO_2 production regime. This is different from the situation on extended Pd(100) surfaces where the oxide is compeletely reduced during the low CO_2 production part of the oscillation cycle. The explanation for this difference could be a size dependent oxidation of the Pd nanoparticles [113, 127]. The larger particles reduce more easily than the smaller particles in this scenario, causing the larger particles to participate in the oscillations and small particles to remain oxidized. This scenario is unlikely because for particles of 15 nm in diameter no significant size effect is observed in ref. [113]. Another more likely explanation is the formation of an interface oxide between the SiO_2 and the Pd nanoparticles [113, 127]. A scenario where this interface oxide is not participating in the oscillations could then explain the remaining PdO intensity in our measurements. We observed that the remaining PdO was reduced in a pure CO atmosphere after the oscillations.

The apparent size of the particles during the reaction oscillations can be determined from the Scherrer equation:

$$\tau = \frac{K\lambda}{\beta_{\mathrm{FWHM}}\cos(\theta)}, \tag{5.1}$$

where τ is a linear dimension of the particles, K is the Scherrer constant, λ is the x-ray wavelength, β_{FWHM} is the FWHM of the diffraction peak in radians, and θ is the Bragg angle [128]. The Scherrer constant K relates the apparent particle size given by:

$$\varepsilon = \frac{\lambda}{\beta_{\mathrm{FWHM}}\cos(\theta)}, \tag{5.2}$$

to a linear dimension of the particle τ via a volume average of the thickness of the particle as measured perpendicular to the reflecting planes [128]. The Scherrer constant K thus depends on the shape of the particle, but it also depends on

the size distribution of the particles [129] and on the way the peak width is determined. Since the shape and the size distribution during the measurement is not accurately known we choose to show only the apparent size of the particles. This apparent size of the metallic part of the particles can be seen to oscillate between 11.5 nm and 12.5 nm. The systematic error in the determination of the apparent size is 0.8 nm. The Scherrer constant for converting apparent size as determined from using β_{FWHM} to the particle diameter, assuming a spherical shape, is 0.84. Also accounting for the width of the size distribution determined after the experiment (Fig. 5.5) would change the Scherrer constant to 0.77. The real size of the (metallic core of the) particles can thus differ substantially from the apparent size. The 1 nm variation in apparent size is converted to a 0.77 nm variation of the particle size. Note that we measured the thickness off the particles in the direction 8.5° off the surface normal of the SiO_2 support. The intensity variations in Fig. 5.3 and Fig. 5.4 together with the assumption of spherical particles with an average radius of 7.5 nm are consistent with the a formation and reduction of a 0.8 nm PdO shell during the oscillations.

The the measurements are thus consistent with the interface oxide scenario where the particles are metallic with an interface oxide underneath the particles in the regime of low CO_2 production and they adopt the form of a smaller metallic core within an oxide shell and an interface oxide underneath the particles in high CO_2 production regime. Apart from the remaining oxide the presence of an interface oxide, this scenario is analogous to that on the extended Pd(100) surface.

It is likely that the synchronization of the oscillations over the whole sample is caused by concentration changes in the CO pressure close to the sample. If one particle switches from the metallic to the more active oxidic phase, locally the CO pressure drops and the surrounding particles are also forced to oxidise. Conversely, if all the particles are oxidized, and one particle switches to the metallic phase the CO pressure locally increases, thereby forcing the surrounding particles to reduce.

Since the oxidation of the particles could be accompanied by shape changes, GISAXS measurements were performed to obtain information on the dimensions of the particles during the oscillations. However a narrowly peaked size distribution is of paramount importance for obtaining an accurate GISAXS fit of the average particle radius and height. Figure 5.5 shows a SEM image of the particles supported on SiO_2 after the experiments described above. The exposure of

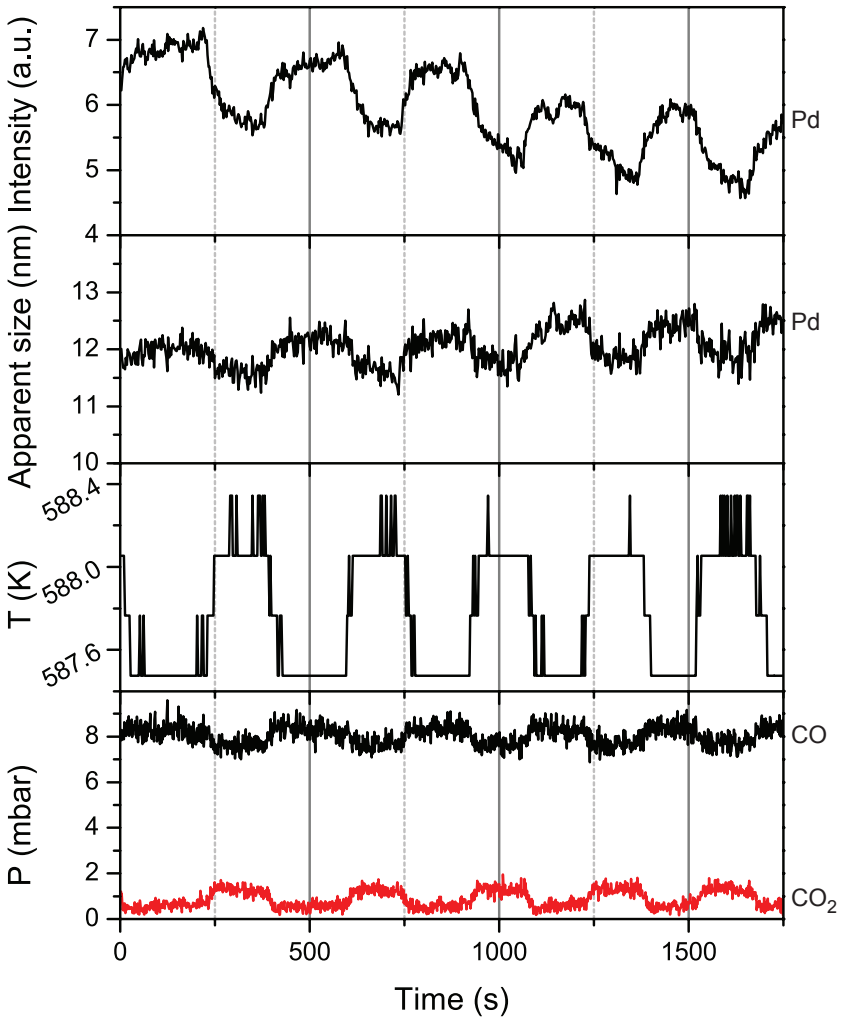

Figure 5.3: Spontaneous oscillations during CO oxidation on the 15 nm diameter Pd particles supported on SiO_2. Measurements were performed in a constant flow of a $CO/O_2/Ar$ gas mixture with an O_2 pressure of 210 mbar, an argon pressure of 281 mbar and a CO pressure of 9 mbar flowing at 50 ml_n min^{-1}. The mass spectrometry signals from CO and CO_2 show that the reaction rate oscillates (lower panel), which in turn makes the temperature vary (third panel). Note that the temperature variations amount to just a few times the least significant bit of the digitized temperature scale. The top two panels show the diffracted intensity from the Pd particles ($2\theta = 17.6°$) and the apparent Pd nanocrystal size, derived from the diffraction line widths.

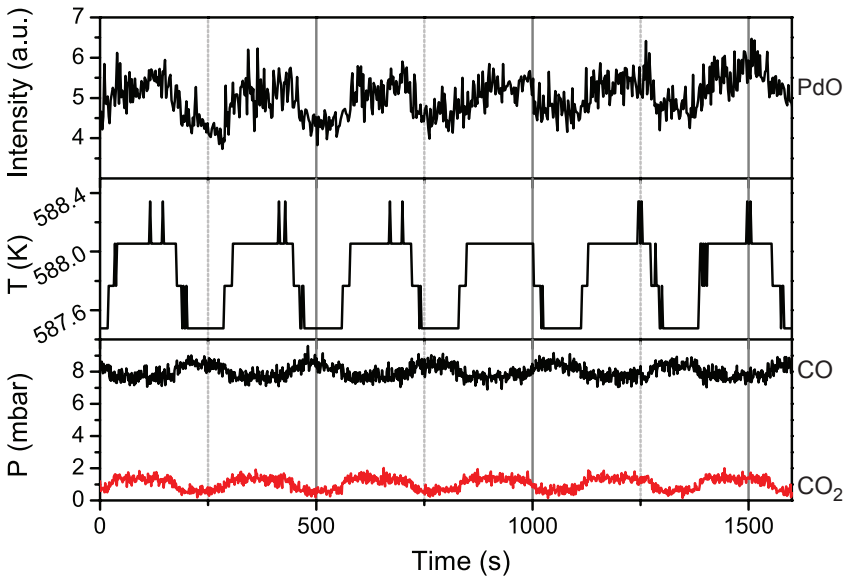

Figure 5.4: Spontaneous oscillations in the CO oxidation rate on the 15 nm diameter Pd particles supported on SiO_2 as measured by XRD and mass spectrometry. Measurements were performed in a constant flow of a CO/O_2/Ar gas mixture with an O_2 pressure of 210 mbar, an argon pressure of 281 mbar and a CO pressure of 9 mbar flowing at 50 ml_n min^{-1}. The mass spectrometry signals from CO and CO_2 show that the reaction rate oscillates (lower panel), which in turn makes the temperature vary second panel). Note that the temperature variations amount to just a few times the least significant bit of the digitized temperature scale. The top panel shows the diffracted intensity from PdO ($2\theta = 14.9°$).

the sample to reactant gasses at high temperatures led to a significant widening of the size distribution from $\frac{\sigma_R}{R} = 0.05$ to $\frac{\sigma_R}{R} = 0.19$, see Fig. 5.5b. Widening of the size distribution can be caused by two effects [130, 131]. The first effect is Ostwald ripening where large particles grow at the expense of smaller particles due to higher vapour pressure of the smaller particles as described by the Gibbs-Thomson equation. The second effect is called Smoluchowski ripening or dynamic coalescence and describes the coarsening caused by diffusion and coalescence of complete particles [132]. From our size distribution we conclude that both Ostwald ripening and Smoluchowski ripening have been important. The importance of Ostwald ripening can be inferred from the fact that we see many par-

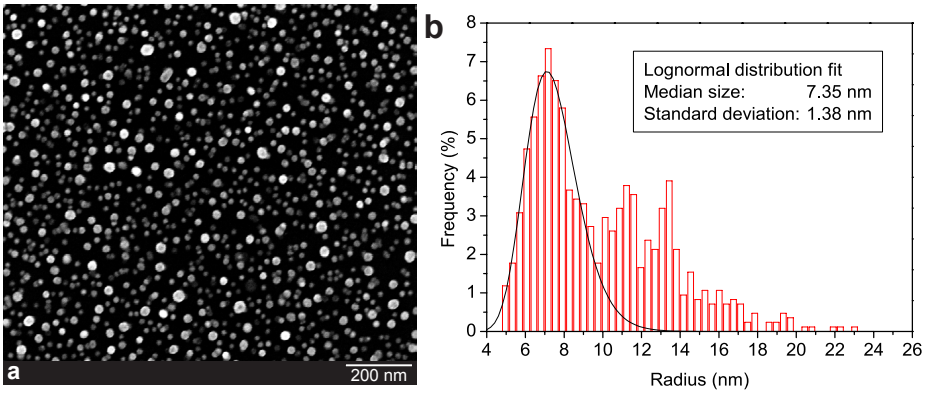

Figure 5.5: a) SEM image of the 15 nm Pd particles deposited on SiO_2. This image was taken after the sample had been in the reactor for the experiments of Figs. 5.1 to 5.4. **b)** Size distribution of the particles as determined from 854 particles in the SEM data after the reaction oscillations.

ticles with a smaller radius than the monodisperse 7.5 nm with which we started. The importance of Smoluchowski ripening can be inferred from the fact that we see multiple peaks in our size distribution at radii that one would expect for either 2, 3, or 4 particles with a 7.5 nm radius coalescing. Fits of the GISAXS for the average particle size for the sample shown in Fig. 5.5 give very large uncertainty in the average radius and height due the the wide size distribution.

Al_2O_3 support

Spontaneous reaction oscillations where also observed for the case of 15 nm Pd particles on Al_2O_3. The intensity variation of the diffracted intensity at a 2θ angle of 17.6° are shown in Fig. 5.6. Assuming the particles are perfectly spherical, the variations in intensity are consistent with the formation and reduction of a 1.0 nm oxide shell during the oscillations. The apparent size is measured 8.5° from the surface normal of the Al_2O_3 and is thus a good measure for the average height of the metallic part of a particle if multiplied by the appropriate Scherrer constant. Assuming the Scherrer constant for a perfect sphere (0.84) the height of the metallic part of a particle varies between 8.8 nm and 9.7 nm. The systematic error in the apparent size determination is 0.8 nm. Intensity variations in the PdO (not shown) signal at $2\theta = 15°$ show the presence of PdO in the high CO_2

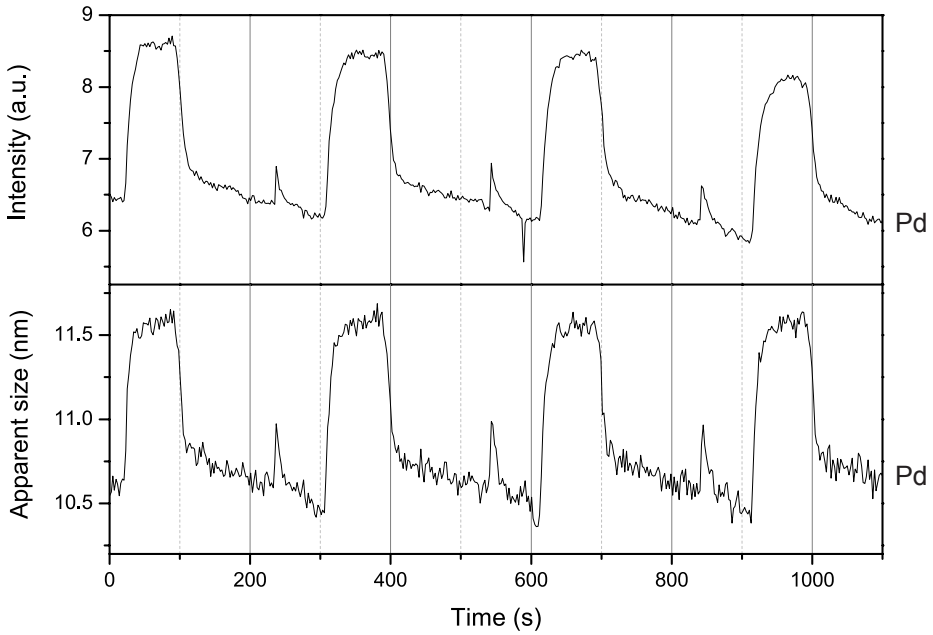

Figure 5.6: Spontaneous oscillations in the CO oxidation rate on the 15 nm diameter Pd particles supported on Al_2O_3. Measurements were performed in a constant flow of a CO/O_2/Ar gas mixture with an O_2 pressure of 210 mbar, an Ar pressure of 281 mbar and a CO pressure of 9 mbar flowing at 50 ml_n min^{-1}. The two panels show the diffracted intensity from the Pd particles ($2\theta = 17.6°$) and the apparent Pd nanocrystal size, derived from the diffraction line widths.

production regime, but PdO is not observed in the low CO_2 production regime.

The size distribution of the 15 nm Pd particles supported on Al_2O_3 remained narrower ($\frac{\sigma_R}{R} \approx 0.1$) during the oscillations and thus resulted in a more meaningful fit of the particle dimensions than for the particles supperted on SiO_2. The non-conducting Al_2O_3 substrate however, caused charging of the particles in the scanning electron microscope preventing a determination of the size distribution by SEM. Figure 5.7 shows reaction oscillations of the Pd nanoparticles supported on Al_2O_3. At four points in this scan GISAXS data were analysed: (1) just before the switch to low CO_2 production, (2) directly after the switch from high to to low CO_2 production, (3) just before the switch to high CO_2 production,(4) directly after the switch to high CO_2 production.

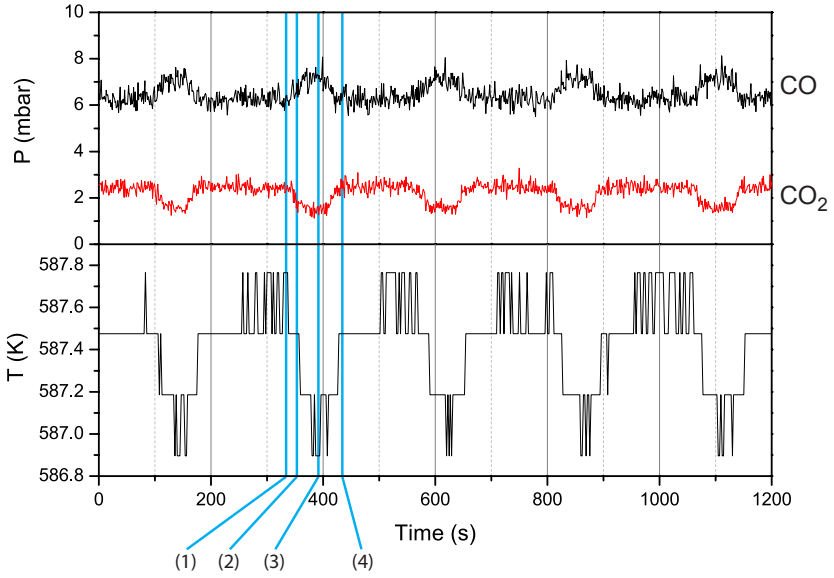

Figure 5.7: Top panel: spontaneous oscillations in the CO oxidation rate on the 15 nm diameter Pd particles supported on Al_2O_3 as measured by mass spectrometry. Bottom panel: sample temperature. Measurements were performed in a constant flow of a CO/O_2/Ar gas mixture with an O_2 pressure of 210 mbar, an Ar pressure of 281 mbar and a CO pressure of 9 mbar flowing at 50 ml_n min^{-1}.

A selection of the GISAXS data and the GISAXS fits are shown in Fig. 5.8. The fits were made using the IsGISAXS progam [133]. The fit of the particle dimensions was made assuming that the particles consist fully of Pd in both phases. From the diffraction data we know that this assumption is not completely justified, since some part of the Pd in the particles is transformed to PdO. In principle we would like to know whether an oxide shell exists around the particles and how thick this shell is, or where the oxide is located otherwise. Ideally we would prefer to base our fits on a geometry in which the PdO is added as a layer of homogeneous thickness on a Pd core, while the amount of Pd is conserved. Such a non-linear constraint is difficult to impose using the IsGISAXS program, so instead we chose to make a fit of the dimensions of the particles, assuming the particles are truncated spheres and a have constant density throughout. The

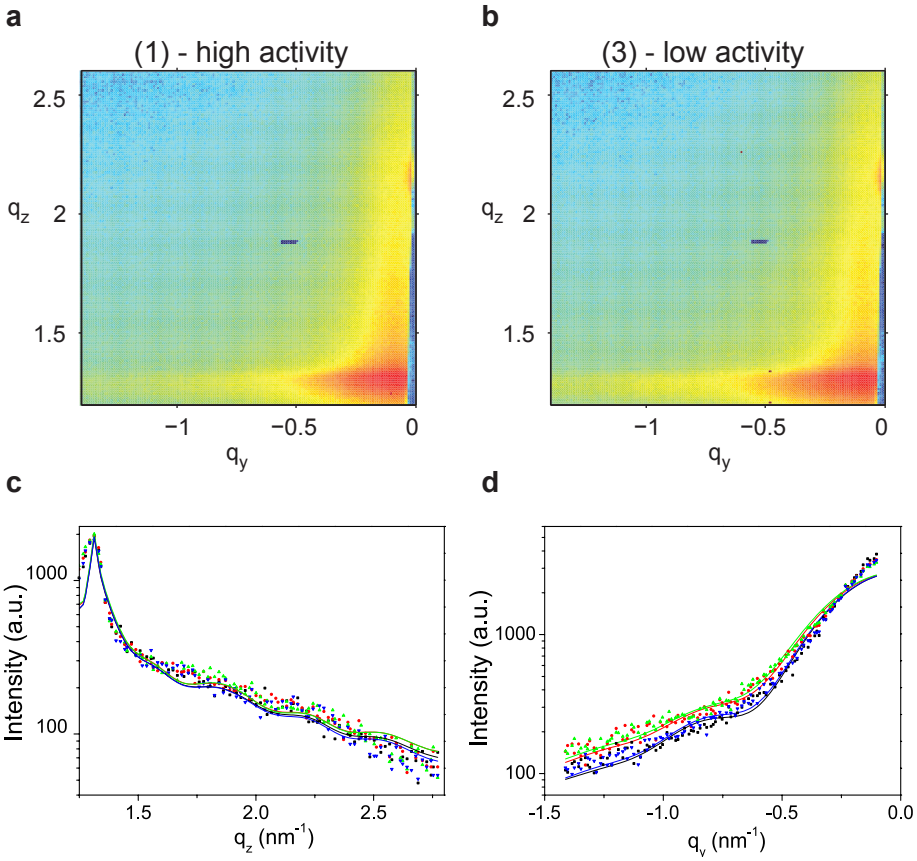

Figure 5.8: GISAXS data and fits at the times indicated in Fig. 5.7. **a)** GISAXS data taken in the high CO_2 production phase at (1) in Fig. 5.7, **b)** GISAXS data taken in the low CO_2 production phase at (3) in Fig. 5.7. **c)** Perpendicular cross section of GISAXS data (1)-black, (2)-red, (3)-green, (4)-blue and fits **d)** Parallel cross section of GISAXS data (1-4) and fits.

GISAXS patterns change most during the switch from high to low CO_2 production and back. Most change is visible in the extent of the Yoneda peak in the q_y direction, which is reduced in the high-activity phase. This change can be fitted well width a modest change of the average particle radius. The best-fit parameters are shown in Table 5.1. H is not a fit parameter, but is calculated from H/R and R. The particles are slightly larger in the high CO_2 production phase. This is consistent with a scenario where the particles are partly oxidized in the high reactivity regime, because the partial oxidation should cause a volume increase of the particles. Note that a radius increase of the particle by 0.16 nm between (3) and (4) in Table 5.1 means that the oxide is a factor $\rho_{\mathrm{Pd}}/(\rho_{\mathrm{Pd}} - \rho_{\mathrm{PdO}}) \approx 3$ thicker. The 0.16 nm increase in radius from the GISAXS fits thus indicates that a ~ 0.5 nm thin oxide exists on the particle during the high CO_2 production, that thickness corresponds to two layers of PdO(101). We note that the uncertainty in the determination of the radius is much larger than this 0.16 nm and interpret the radius increase merely as a qualitative effect.

Assuming a spherical shape, these fit results also seem to suggest that the contact angle of the particles with the Al_2O_3 substrate is slightly smaller in the high reactivity regime. We would like to stress that what we measure and fit is the average behaviour of the ensemble of particles. The measurements do not exclude a scenario in which for example small particles are covered in a thicker oxide than large particles.

Table 5.1: GISAXS parameters for the fits in Fig. 5.8 to the data obtained at the four times (1)-(4) indicated in Fig. 5.7. R is the average particle radius,σ_R the standard deviation of the radius and H the average height.

	R (nm)	$\frac{\sigma_R}{R}$	H (nm)	$\frac{H}{R}$
(1)	7.49 ± 0.88	9.63×10^{-2}	13.41 ± 2.40	1.79 ± 0.11
(2)	7.40 ± 1.03	9.94×10^{-2}	13.47 ± 2.54	1.82 ± 0.09
(3)	7.32 ± 1.11	1.02×10^{-1}	13.40 ± 2.69	1.83 ± 0.09
(4)	7.48 ± 0.87	9.51×10^{-2}	13.46 ± 2.31	1.80 ± 0.10

When we compare the height of the particles of (13.4 ± 2.4) nm as determined by GISAXS with the height from the diffraction line widths of (9.7 ± 0.8) nm we find a discrepancy of 3.7 nm. The existence of an interface compound consisting could account for this discrepancy. Since we do not detect PdO in the diffraction

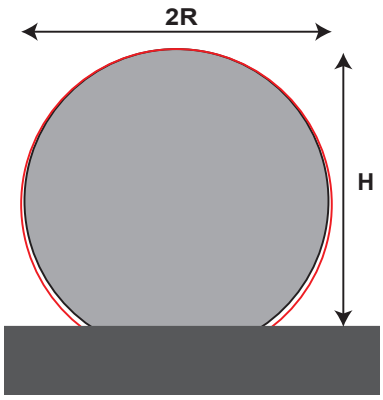

Figure 5.9: Black: average shape of the Pd particles in the low CO_2 production phase as determined by GISAXS. Red: average shape of the partly oxidized Pd particles in the high CO_2 production phase as determined by GISAXS.

data in the low CO_2 production regime, we suspect that we are dealing with Pd aluminate interface compound.

Furthermore we observed an influence of the presence of the x-ray beam on the period of the oscillations. Removal of the x-ray beam during the oscillations resulted in an increase of the oscillation period from 3.0×10^2 s to 7.0×10^2 s . We also observe a temperature decrease of 1.2 °C after removal of the beam and an increase in the temperature amplitude of the oscillations from 0.7 °C to 1.2 °C. Changing the temperature by this amount without removing the beam did not result in a change of the oscillation period. The x-rays thus have a real effect on the speed of the oscillations. The increase in the temperature amplitude suggests a larger difference in reactivity between the high and low CO_2 production parts of an oscillation period. The high CO_2 production part of the oscillation period is mass transfer limited, so we only expect to see slightly lower CO_2 signal in the low CO_2 production part of the period, compared to the situation with presence of the x-ray beam. Such an effect is indeed visible in the mass spectrometer.

5.4 Conclusion

We have shown that significant amounts of bulk-like PdO are only present on supported 15 nm particles if we pre-oxidise the particles, before doing the steady state reactivity measurements and that the detection of surface oxides on nanoparticles under catalytic conditions remains a challenge.

We have also shown that 15 nm Pd particles supported on Al_2O_3 and SiO_2 show self sustained reaction oscillations. During these oscillations the particles go from a metallic to a partly oxidized state and they change radius. The measurements are consistent with the formation and reduction of a 0.5 nm to 1.0 nm thick PdO shell around a Pd core. A marked difference between the oscillations exhibited by the nanoparticles supported on SiO_2 with the oscillations on single-crystal Pd(100) is that on the nanoparticle samples part of the PdO is not reduced in the low CO_2 production regime. An interface oxide between the particles and the substrate could explain this difference. For the Pd particles supported on Al_2O_3 an interface compound between the particle and the substrate also seems to be present, but the structure of this compound could not be determined. The driving mechanism for the oscillations could be similar to the roughening mechanism on the Pd(100) single crystal. Unfortunately probing the roughness, or perhaps more appropriately, the degree of imperfection, of and oxide covering a particle, remains an experimental challenge. We believe that the use of supported monodisperse nanoparticles in combination with XRD and GISAXS constitutes a powerful method of studying the in situ shape of nanoparticles.